Journal of Zhejiang University-SCIENCE A (Applied Physics & Engineering)
ISSN 1673-565X (Print); ISSN 1862-1775 (Online)
www.zju.edu.cn/jzus; www.springerlink.com
E-mail: jzus@zju.edu.cn

Large eddy simulation for wind field analysis based on stabilized finite element method*

Cheng HUANG, Yan BAO, Dai ZHOU‡, Jin-quan XU

(*School of Naval Architecture, Ocean and Civil Engineering, Shanghai Jiao Tong University, Shanghai 200240, China*)

E-mail: ryanhuang@sjtu.edu.cn; ybao@sjtu.edu.cn; zhoudai@sjtu.edu.cn; jqxu@sjtu.edu.cn

Received Mar. 26, 2010; Revision accepted Sept. 2, 2010; Crosschecked Mar. 1, 2011

Abstract: In this paper, a stabilized finite element technique, actualized by streamline upwind Petrov-Galerkin (SUPG) stabilized method and three-step finite element method (FEM), for large eddy simulation (LES) is developed to predict the wind flow with high Reynolds numbers. Weak form of LES motion equation is combined with the SUPG stabilized term for the spatial finite element discretization. An explicit three-step scheme is implemented for the temporal discretization. For the numerical example of 2D wind flow over a square rib at Re=4.2×10^5, the Smagorinsky's subgrid-scale (SSGS) model, the DSGS model, and the DSGS model with Cabot near-wall model are applied, and their results are analyzed and compared with experimental results. Furthermore, numerical examples of 3D wind flow around a surface-mounted cube with different Reynolds numbers are performed using DSGS model with Cabot near-wall model based on the present stabilized method to study the wind field and compared with experimental and numerical results. Finally, vortex structures for wind flow around a surface-mounted cube are studied by present numerical method. Stable and satisfactory results are obtained, which are consistent with most of the measurements even under coarse mesh.

Key words: Large eddy simulation (LES), Subgrid-scale model, Stabilized finite element method (FEM), Unstructured grid, Wind flow

doi:10.1631/jzus.A1000114 **Document code:** A **CLC number:** TU31

1 Introduction

Arising from the importance of engineering applications of wind flow around structures, numerical computation is becoming more and more widely used due to the progress in computational fluid dynamics (CFD) techniques and computer science over the past few decades. The wind field around the obstacle on the ground consists of a very complex 3D turbulent vortex structure. Among a number of existing numerical techniques in CFD for predicting wind flow, large-eddy simulation (LES) appears to be one of the most promising approaches in practical applications. In LES, the fluctuating motions of turbulence can be computed except for those eddies that are smaller than the grid size, while the smaller eddies are modeled using eddy viscosity models. Early LES computation was based on the Smagorinsky model for the unresolved subgrid-scales (SGS) (Smagorinsky, 1963), which is still widely used in many fields (Uchida and Ohya, 2003; Itoh and Tamura, 2008; Jimenez *et al*., 2008). However, it is impossible to simulate the flow effectively with a single, universal constant C_s in the model. The SGS eddy viscosity extrapolated to the wall is not desirable, and the Smagorinsky model cannot account for energy flow from small scales to large scales. To overcome these drawbacks, a dynamic SGS model has been proposed (Germano *et al*., 1991; Lilly, 1992).

‡ Corresponding author

* Project supported by the National Natural Science Foundation of China (No. 51078230), the Research Fund for the Doctoral Program of Higher Education of China (No. 200802480056), and the Key Project of Fund of Science and Technology Development of Shanghai (No. 10JC1407900), China

Historically, LES has been restricted to simple geometries, where finite volume method and finite difference methods can be conveniently used due to their efficient use of structured grids. However, structured grids not only have difficulty in representing complex domains and adapting to complicated flow features, but also are rather inefficient for simulating flow at a high Reynolds number (Moin and Jimenéz, 1993). To gain the advantages of dealing with complex geometry and boundary conditions, a finite element method (FEM) has been widely used for the solution of various fluid dynamic problems. Unstructured grids in FEM can locate a large number of nodes and elements near the wall and form coarseness of grids in all directions away from the wall due to the fact that the elements grow not only in the normal direction but also in the other directions. This greatly reduces the total number of nodes and elements required for a given turbulent problem (Jansen, 1994).

However, it is known that the classic Galerkin FEM has great problems in prediction when applied to solving fluid flows with a high Reynolds number. In order to overcome this drawback, stabilized finite element formulations have been developed, among which, a streamline upwind Petrov-Galerkin (SUPG) method is very efficient. This was proposed by Brooks and Hughes (1982), and further developed by Hughes *et al*. (1986) and Tezduyar (2007).

The present calculations are undertaken using a stabilized finite element technique implemented by a three-step FEM and SUPG stabilized method for LES to predict the wind flow with a high Reynolds number. The same order interpolations for the velocity and pressure are employed for the spatial discretization, and the explicit three-step FEM is applied for the temporal discretization. A simple filtering procedure using both node-based filter and generalized box filter is applied for the dynamic subgrid-scale (DSGS) model with unstructured grids. For the verification of the present numerical method, the predictions of 2D wind flow over a square rib at Re=4.2×10^5 and 3D wind flow around a surface-mounted cube at different Reynolds numbers are simulated by the present DSGS technique with Cabot near-wall model to study the wind field. The results predicted by the present method are compared with experimental data and analyzed for the characteristics of the wind field.

2 Governing equations

2.1 Non-dimensionalized Navier-Stokes equations

The governing equations of the wind flow can be described by the continuity and momentum equations. Using the non-dimensionalized variables, and describing the problem by a Reynolds number defined as $Re=UD/v$, where U and D are the characteristic velocity and length, and v is the kinematic viscosity, the non-dimensionalized Navier-Stokes equation can be written in Cartesian tensor notation as follows:

$$\frac{\partial u_i}{\partial x_i}=0, \tag{1}$$

$$\frac{\partial u_i}{\partial t}+\frac{\partial u_i u_j}{\partial x_j}=-\frac{\partial p}{\partial x_i}+\frac{1}{Re}\frac{\partial^2 u_i}{\partial x_j \partial x_j}, \tag{2}$$

where u_i is the velocity in i direction, t is the time, and p is the pressure.

In LES, the large scale quantities are resolved, while the small scale quantities are modeled. The large scale quantities are defined by the convolution of the velocity and pressure fields with a filter function. A grid filter $\overline{G}$ is applied to the continuity and momentum equations:

$$\overline{f}(x)=\int f(x')\overline{G}(x,x')\mathrm{d}x', \tag{3}$$

where x' is the integral range, $f(x')$ is the variable before the filtering process, and $\overline{f}(x)$ is the variable after the filtering process. This gives the filtered equations of motions corresponding to Eqs. (1) and (2):

$$\frac{\partial \overline{u}_i}{\partial x_i}=0, \tag{4}$$

$$\frac{\partial \overline{u}_i}{\partial t}+\frac{\partial \overline{u}_i \overline{u}_j}{\partial x_j}=-\frac{\partial \overline{p}}{\partial x_i}-\frac{\partial \tau_{ij}}{\partial x_j}+\frac{1}{Re}\frac{\partial^2 \overline{u}_i}{\partial x_j \partial x_j}, \tag{5}$$

where $\overline{u}_i$, $\overline{u}_j$, and $\overline{p}$ are the variables after the filtering process, corresponding to u_i, u_j, and p, respectively. The effects of the small scales appear in the subgrid-scale stress term τ_{ij}, which must be modeled:

$$\tau_{ij}=\overline{u_iu_j}-\overline{u}_i\overline{u}_j, \tag{6}$$

where $\overline{u_iu_j}$ is the filtered variable of u_iu_j.

2.2 Smagorinsky subgrid-scale (SSGS) model

The eddy viscosity model is frequently used to represent the effects of SGS in LES. τ_{ij} is assumed to be a non-linear function of the strain rate, and it may be written as (Smagorinsky, 1963)

$$\tau_{ij}=-2\nu_{\mathrm{t}}\overline{S}_{ij}, \tag{7}$$

$$\overline{S}_{ij}=\frac{1}{2}\left(\frac{\partial\overline{u}_i}{\partial x_j}+\frac{\partial\overline{u}_j}{\partial x_i}\right), \tag{8}$$

$$\nu_{\mathrm{t}}=(C_{\mathrm{s}}\overline{\Delta})^2\left|\overline{S}\right|, \tag{9}$$

$$\left|\overline{S}\right|=\sqrt{2\overline{S}_{ij}\overline{S}_{ij}}, \tag{10}$$

where $\overline{S}_{ij}$ is the filtered strain rate component, and ν_{t} is the eddy viscosity. C_{s} is the Smagorinsky constant and the value of 0.1 is used here as suggested by Deardorff (1970). $\overline{\Delta}$ is the grid filter width, the value of which is the square root of the area of the unstructured element for the present 2D case.

2.3 Dynamic subgrid-scale (DSGS) model

In the SSGS model, C_{s} has a constant value over the whole domain during the time progressing process. By contrast, in the dynamic subgrid-scale model, the constant C varies in both space and time domains without any interference by the user, and is proved to have better behavior near walls.

For the DSGS model, a test filter $\tilde{G}$, denoted by a tilde, is defined as

$$\tilde{f}(x)=\int f(x')\tilde{G}(x,x')\mathrm{d}x', \tag{11}$$

where $\tilde{f}(x)$ is the variable after the second filtering process. Applying Eq. (11) to Eq. (5), the second filtered Navier-Stokes equation becomes

$$\frac{\partial\tilde{\overline{u}}_i}{\partial t}+\frac{\partial\tilde{\overline{u}}_i\tilde{\overline{u}}_j}{\partial x_j}=-\frac{\partial\tilde{\overline{p}}}{\partial x_i}-\frac{\partial T_{ij}}{\partial x_j}+\frac{1}{Re}\frac{\partial^2\tilde{\overline{u}}_i}{\partial x_j\partial x_j}, \tag{12}$$

where $\tilde{\overline{u}}_i$, $\tilde{\overline{u}}_j$, and $\tilde{\overline{p}}$ are the variables after the second filtering process, corresponding to $\overline{u}_i$, $\overline{u}_j$, and $\overline{p}$, respectively, and the subgrid-scale stress T_{ij} is

$$T_{ij}=\widetilde{\overline{u_iu_j}}-\tilde{\overline{u}}_i\tilde{\overline{u}}_j, \tag{13}$$

where $\widetilde{\overline{u_iu_j}}$ is the variable after the second filtering process corresponding to $\overline{u_iu_j}$, and the resolved turbulent stress L_{ij} can be defined as

$$L_{ij}=T_{ij}-\tilde{\tau}_{ij}, \tag{14}$$

$$L_{ij}=\widetilde{\overline{u}_i\overline{u}_j}-\tilde{\overline{u}}_i\tilde{\overline{u}}_j, \tag{15}$$

where $\tilde{\tau}_{ij}$ and $\widetilde{\overline{u}_i\overline{u}_j}$ are the filtered variables of τ_{ij} and $\overline{u}_i\overline{u}_j$, respectively. L_{ij} represents the contribution to the Reynolds stresses by the scales, whose length is intermediate between the grid and the test filter widths (Germano *et al*., 1991). The subgrid-scale stress tensors can be modeled using traditional turbulent viscosity:

$$\tau_{ij}-(\delta_{ij}/3)\tau_{kk}=-2(C\overline{\Delta})^2\left|\overline{S}\right|\overline{S}_{ij}, \tag{16}$$

$$T_{ij}-(\delta_{ij}/3)T_{kk}=-2(C\tilde{\overline{\Delta}})^2\left|\tilde{\overline{S}}\right|\tilde{\overline{S}}_{ij}, \tag{17}$$

$$\tilde{\overline{S}}_{ij}=\frac{1}{2}\left(\frac{\partial\tilde{\overline{u}}_i}{\partial x_j}+\frac{\partial\tilde{\overline{u}}_j}{\partial x_i}\right), \tag{18}$$

$$\left|\tilde{\overline{S}}\right|=\sqrt{2\tilde{\overline{S}}_{ij}\tilde{\overline{S}}_{ij}}, \tag{19}$$

where δ_{ij} is the identity tensor, $\tilde{\overline{\Delta}}$ is the characteristic size of the filter $\tilde{\overline{G}}$, and $\tilde{\overline{S}}_{ij}$ is the strain rate tensor of the velocity fields associated with the test filter.

A key variable for the DSGS model is defined as

$$M_{ij}=\widetilde{\left|\overline{S}\right|\overline{S}_{ij}}-\alpha\left|\tilde{\overline{S}}\right|\tilde{\overline{S}}_{ij}, \tag{20}$$

where $\widetilde{\left|\overline{S}\right|\overline{S}_{ij}}$ is the filtered variable of $\left|\overline{S}\right|\overline{S}_{ij}$, α is the square value of the filter width ratio, and $\alpha=(\tilde{\overline{\Delta}}/\overline{\Delta})^2$. Here we set α=4, since the size of the filter $\tilde{G}$ is twice that of $\overline{G}$ (Tejada-Martínez and Jansen, 2004).

Based on Eqs. (14), (16), (17), and (20), and using a simple least-squares minimization of the error first proposed by Lilly (1992), the constant C in Eqs. (16) and (17) can be confirmed by

$$(C\bar{\Delta})^2=\frac{1}{2}\left(\frac{L_{ij}M_{ij}}{M_{ij}M_{ij}}\right). \tag{21}$$

Substituting Eq. (16) into Eq. (5) and considering the incompressible condition, motion equations can be expressed as

$$\frac{\partial\bar{u}_i}{\partial x_i}=0, \tag{22}$$

$$\frac{\partial\bar{u}_i}{\partial t}+\bar{u}_j\frac{\partial\bar{u}_i}{\partial x_j}=-\frac{\partial\bar{P}}{\partial x_i}+\left(\frac{1}{Re}+\nu_{\mathrm{t}}\right)\frac{\partial^2\bar{u}_i}{\partial x_j\partial x_j}, \tag{23}$$

where $\bar{u}_i$ is the filtered velocity of i direction, $\bar{P}$ is the effective pressure, $\bar{P}=\bar{p}+\tau_{kk}$, and the turbulent viscosity can be described as

$$\nu_{\mathrm{t}}=(C\bar{\Delta})^2\left|\bar{S}\right|. \tag{24}$$

Following this procedure, the length scale squared $(C\bar{\Delta})^2$ is dynamically determined to be a function of both space and time.

3 Filtering progress for unstructured grids

To reduce the data storage of the filtering process, a technique combined by the node-based filter and generalized box filter, which are applied by Popiolek *et al*. (2006) and Jansen (1999), is implemented to calculate the key values of L_{ij} and M_{ij} in Eqs. (15) and (20), respectively. The filtering variable of a specific node can be obtained by calculating the mean value of the surrounding nodes or the surrounding elements:

$$\widetilde{\bar{u}_i\bar{u}_j}=\frac{1}{n}\sum_{i=1}^{n}\bar{u}_i\bar{u}_j, \tag{25}$$

$$\tilde{\bar{u}}_i=\frac{1}{n}\sum_{i=1}^{n}\bar{u}_i, \tag{26}$$

where $\widetilde{\bar{u}_i\bar{u}_j}$ and $\tilde{\bar{u}}_i$ are the filtered variables of the specific node, $\bar{u}_i\bar{u}_j$ and $\bar{u}_i$ are the same variables belonging to the nodes connected with the specific node, n is the number of these nodes, and

$$\tilde{\bar{S}}_{ij}=\frac{1}{m}\sum_{i=1}^{m}\bar{S}_{ij}, \tag{27}$$

$$\left|\tilde{\bar{S}}\right|=\frac{1}{m}\sum_{i=1}^{m}\left|\bar{S}\right|, \tag{28}$$

$$\widetilde{\left|\bar{S}\right|\bar{S}_{ij}}=\frac{1}{m}\sum_{i=1}^{m}\left|\bar{S}\right|\bar{S}_{ij}, \tag{29}$$

where $\tilde{\bar{S}}_{ij}$, $\left|\tilde{\bar{S}}\right|$, and $\widetilde{\left|\bar{S}\right|\bar{S}_{ij}}$ are the filtered variables of the specific node, $\bar{S}_{ij}$, $\left|\bar{S}\right|$, and $\left|\bar{S}\right|\bar{S}_{ij}$ are the same variables belonging to the elements sharing the specific node as a vertex, and m is the number of these elements.

4 Stabilized finite element method

4.1 Finite element discretization with SUPG method

Here we elide the superscript overbar in Eqs. (22) and (23) and omit the stress boundary conditions. The stabilized finite element discretization of the filtered equation Eq. (23) can be expressed by multiplying the velocity test function δu_i and adding SUPG stabilized term as follows (Brooks and Hughes, 1982):

$$\int_{\Omega}\left[\delta u_i\left(\frac{\partial u_i}{\partial t}+u_j\frac{\partial u_i}{\partial x_j}\right)+\sigma_{ij}\frac{\partial\delta u_{\mathrm{i}}}{\partial x_j}\right]\mathrm{d}\Omega$$
$$+\sum_{n=1}^{n_{\mathrm{el}}}\int_{\Omega}\tau_{\mathrm{SUPG}}u_j\frac{\partial\delta u_{\mathrm{i}}}{\partial x_j}\left(\frac{\partial u_i}{\partial t}+u_j\frac{\partial u_i}{\partial x_j}-\frac{\partial\sigma_{ij}}{\partial x_j}\right)\mathrm{d}\Omega=0, \tag{30}$$

where Ω is the computational domain, n_{el} is the number of elements, δu_i is the velocity test function, σ_{ij} is the filtered stress tensor expressed by

$$\sigma_{ij}=-P\delta_{ij}+\left(\frac{1}{Re}+\nu_{\mathrm{t}}\right)\left(\frac{\partial u_i}{\partial x_j}+\frac{\partial u_j}{\partial x_i}\right), \tag{31}$$

and the stabilization parameter τ_{SUPG} is defined as follows (Dettmer and Peric, 2006):

$$\tau_{\mathrm{SUPG}}=\frac{h^{\mathrm{e}}}{2\left\|u^{\mathrm{e}}\right\|}z,$$
$$z=\frac{\beta_1}{\sqrt{1+(\beta_1/\beta_2 Re^{\mathrm{e}})^2}},$$
$$Re^{\mathrm{e}}=\frac{\left\|u^{\mathrm{e}}\right\|h^{\mathrm{e}}}{2\nu}, \tag{32}$$

where h^{e}, u^{e}, and Re^{e} represent the characteristic size, convective velocity, and the Reynolds number of an element, respectively. β_1 defines the limits of z as Re^{e} nears infinity, and β_2 defines the derivative $\frac{\mathrm{d}z}{\mathrm{d}Re^{\mathrm{e}}}$ at $Re^{\mathrm{e}}=0$, where z is a process parameter. In this work, $\beta_1=1$ and $\beta_2=1/3$ have been used, and the characteristic element size is defined as the diameter of a circle (or a sphere) whose area (or volume) is equal to the element area (or volume) for the 2D (or 3D) model.

The finite element discretization of Eq. (30) is performed using the same order interpolations of velocity and pressure. For the present study, three-node linear triangular elements for the 2D model and four-node linear tetrahedral elements for the 3D model are employed. The values of velocity and pressure in an element can be obtained from

$$u_i=\Phi_I u_{iI},\quad P=\Phi_I P_I, \tag{33}$$

where u_{iI} is the i-directional velocity at node I, P_I is the pressure at node I, and Φ_I is the trial and shape function.

Substituting Eq. (33) into Eq. (30), the finite element formulation for the momentum equation is expressed as follows:

$$M_{IJ}\frac{\partial u_{iJ}}{\partial t}+N_{IJ}u_{iJ}-G_{iIJ}P_J+H_{iI}+D_{IJ}u_{iJ}=0, \tag{34}$$

where the basis matrix variables are obtained as

$$M_{IJ}=\int_\Omega \Phi_I\Phi_J\mathrm{d}\Omega+\tau_{\mathrm{SUPG}}\int_\Omega\frac{\partial\Phi_I}{\partial x_j}\Phi_J\Phi_K u_{jK}\mathrm{d}\Omega, \tag{35}$$

$$N_{IJ}=\int_\Omega \Phi_I u_{iK}\Phi_K\frac{\partial\Phi_J}{\partial x_i}\mathrm{d}\Omega+\tau_{\mathrm{SUPG}}\int_\Omega\frac{\partial\Phi_I}{\partial x_j}\Phi_L u_{jL}\Phi_K u_{jK}\Phi_{jJ}\mathrm{d}\Omega, \tag{36}$$

$$G_{iIJ}=\frac{1}{\rho}\int_\Omega\frac{\partial\Phi_I}{\partial x_i}\Phi_J\mathrm{d}\Omega-\tau_{\mathrm{SUPG}}\frac{1}{\rho}\int_\Omega\frac{\partial\Phi_I}{\partial x_{\mathrm{j}}}\Phi_K u_{jK}\frac{\partial\Phi_J}{\partial x_i}\mathrm{d}\Omega, \tag{37}$$

$$H_{iI}=\left(\frac{1}{\mathrm{Re}}+\nu_{\mathrm{t}}\right)\int_\Omega\frac{\partial\Phi_I}{\partial x_j}\frac{\partial\Phi_J}{\partial x_i}u_{jJ}\mathrm{d}\Omega, \tag{38}$$

$$D_{IJ}=\left(\frac{1}{Re}+\nu_{\mathrm{t}}\right)\int_\Omega\frac{\partial\Phi_I}{\partial x_j}\frac{\partial\Phi_J}{\partial x_j}\mathrm{d}\Omega, \tag{39}$$

where I, J, K, and L are the subscripts for the dimensions, equal to 1 and 2 for the 2D model, and equal to 1−3 for the 3D model.

4.2 Three-step FEM formulations

For the formulation of the momentum equation with SUPG stabilized term described in Eq. (34), we adopt an explicit three-step FEM based on a Taylor series expansion in time (Jiang and Kawahara, 1993). Then, the formulations of the momentum equation at each step can be expressed as

$$M_{IJ}^{n}\frac{u_{iJ}^{n+1/3}-u_{iJ}^{n}}{\Delta t/3}=-N_{IJ}^{n}u_{iJ}^{n}+G_{iIJ}^{n}P_J^{n}-H_{iI}^{n}-D_{IJ}^{n}u_{iJ}^{n}, \tag{40}$$

$$M_{IJ}^{n+1/3}\frac{u_{iJ}^{n+2/3}-u_{iJ}^{n+1/3}}{\Delta t/3}=-N_{IJ}^{n+1/3}u_{iJ}^{n+1/3}+G_{iIJ}^{n+1/3}P_J^{n}-H_{iI}^{n+1/3}-D_{IJ}^{n+1/3}u_{iJ}^{n+1/3}, \tag{41}$$

$$M_{IJ}^{n+2/3}\frac{u_{iJ}^{n+1}-u_{iJ}^{n+2/3}}{\Delta t/3}=-N_{IJ}^{n+2/3}u_{iJ}^{n+2/3}+G_{iIJ}^{n+2/3}P_J^{n+1}-H_{iI}^{n+2/3}-D_{IJ}^{n+2/3}u_{iJ}^{n+2/3}, \tag{42}$$

where Δt represents the length of the time increment, the superscripts 'n+1/3', 'n+2/3', and 'n+1' denote the sub-steps of each time increment, respectively. It is clear that, based on Eqs. (40)–(42), we can obtain $u_i^{n+1/3}$ from u_i^n and P^n, then obtain $u_i^{n+2/3}$ from $u_i^{n+1/3}$ and P^n, after that we have to compute P^{n+1}, and finally we can get u_i^{n+1} from $u_i^{n+2/3}$ and P^{n+1}.

By taking the divergence of Eq. (23) and considering the incompressible condition of Eq. (22), the Poisson pressure equation can be obtained as

$$\frac{\partial^2 P^{n+1}}{\partial x_i \partial x_i} = \frac{1}{\Delta t}\frac{\partial u_i^n}{\partial x_i} - \frac{\partial}{\partial x_i}\left(u_j^{n+1/2}\frac{\partial u_i^{n+1/2}}{\partial x_j}\right) + \left(\frac{1}{Re}+\nu_t\right)\frac{\partial^2}{\partial x_i \partial x_j}\left(\frac{\partial u_i^{n+1/2}}{\partial x_j}+\frac{\partial u_j^{n+1/2}}{\partial x_i}\right), \quad (43)$$

where $u_i^{n+1/2} = (u_i^{n+1/3} + u_i^{n+2/3})/2$.

Substituting the finite element trial function into Eq. (43), the final finite element formulation for pressure P^{n+1} is

$$S_{IJ} P_J^{n+1} = -Q_{iIJ} u_{iJ}^n - R_{iIJ} u_{iJ}^{n+1/2}, \quad (44)$$

where the basis matrix variables are obtained as

$$S_{IJ} = \frac{1}{\rho}\int_\Omega \frac{\partial \Phi_I}{\partial x_i}\frac{\partial \Phi_J}{\partial x_i}\mathrm{d}\Omega, \quad (45)$$

$$Q_{iIJ} = \frac{1}{\Delta t}\int_\Omega \Phi_I \frac{\partial \Phi_J}{\partial x_i}\mathrm{d}\Omega, \quad (46)$$

$$R_{iIJ} = \int_\Omega \frac{\partial \Phi_I}{\partial x_j}\Phi_J \frac{\partial \Phi_K}{\partial x_i} u_{jK}^{n+1/2}\mathrm{d}\Omega. \quad (47)$$

5 Numerical examples

To verify the feasibility of the present method, two test problems on the wind flow are performed. One is a 2D wind flow over a square rib, and the other is a 3D wind flow around a surface-mounted cube.

5.1 Wind flow over a square rib at Re=4.2×10^5

Based on the present stabilized FEM, SSGS, DSGS, and DSGS with near-wall model (DSGS-W) proposed by Cabot (1996) for the element close to the wall are applied to simulate the wind flow over a square rib, and the results are compared with the experimental measurements from Crabb *et al*. (1977).

The forms of the computational domain and finite element mesh are shown in Fig. 1. The characteristic velocity of a streamwise direction from the inlet and the characteristic length of the rib are assumed to be of unit value. The size of computational domain are chosen with x=26.5 and y=8, which are the same as in Young *et al*. (2006). The inlet boundary is on the left side of the obstacle, and the outlet is on the right. The lower boundary corresponds to the wind tunnel wall, and the upper boundary corresponds to a free boundary according to the case. No-slip boundary conditions are imposed along the walls, u=1 and v=0 are prescribed along the inlet boundary and the free boundary, and the wind flow is considered at a Reynolds number of 4.2×10^5 in the present analysis, which is the same as Young *et al*. (2006). On the outer boundary, the pressure is set to be zero. We used 6812 nodes and 13 190 unstructured elements with a refined mesh along the wall, and the smallest size of the mesh is 0.1. Here we used a coarse mesh to show the effectiveness and stability of the present method. A total time of t=200 with a time step of 0.02 is used in the present analysis.

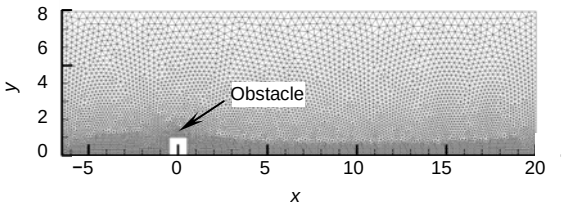

Fig. 1 Calculation domain and finite element mesh

Figs. 2 and 3 show the time-averaged values of streamline distribution and streamwise velocity field of the three cases respectively, for the wind flow in a total time of t=200. As shown in Fig. 2, the flow field consists of flow re-circulations, which are located in front, behind, and on top of the obstacle, and one main re-circulation appears behind the obstacle. Fig. 3 shows that the streamwise velocity field by DSGS-W has a better prediction along the downstream wall due to the Cabot near-wall model with effective capability for LES near the wall.

The time-averaged streamwise velocity profiles at different axial locations of the square rib are compared with the experiment results from Crabb *et al*. (1977) (Fig. 4). When x=−2.5, the results of SSGS, DSGS, and DSGS-W all agree with the experimental results at y>0.5; however, they all lose some accuracy at y<0.5 but with correct trends. For the instance of x=−0.9, the three cases all agree with experimental results at y>1.2; however, they all lose some accuracy

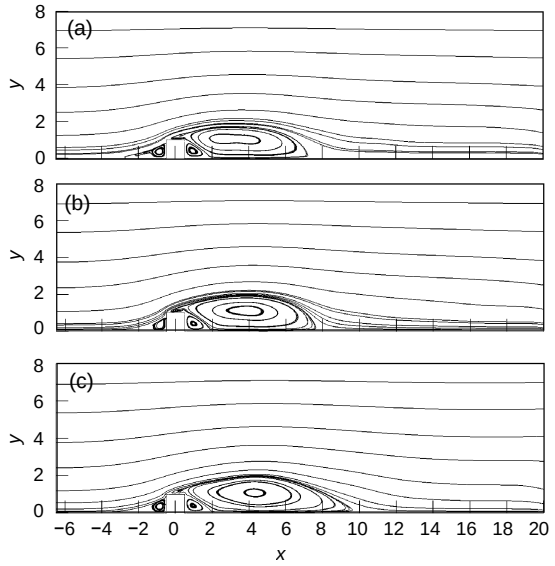

Fig. 2 Mean streamline distribution for flow over a square rib, Re=4.2×10^5
(a) SSGS; (b) DSGS; (c) DSGS-W

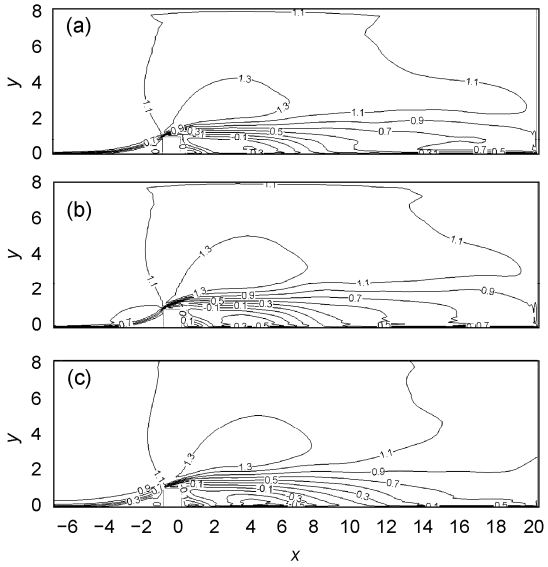

Fig. 3 Mean streamwise velocity field for flow over a square rib, Re=4.2×10^5
(a) SSGS; (b) DSGS; (c) DSGS-W

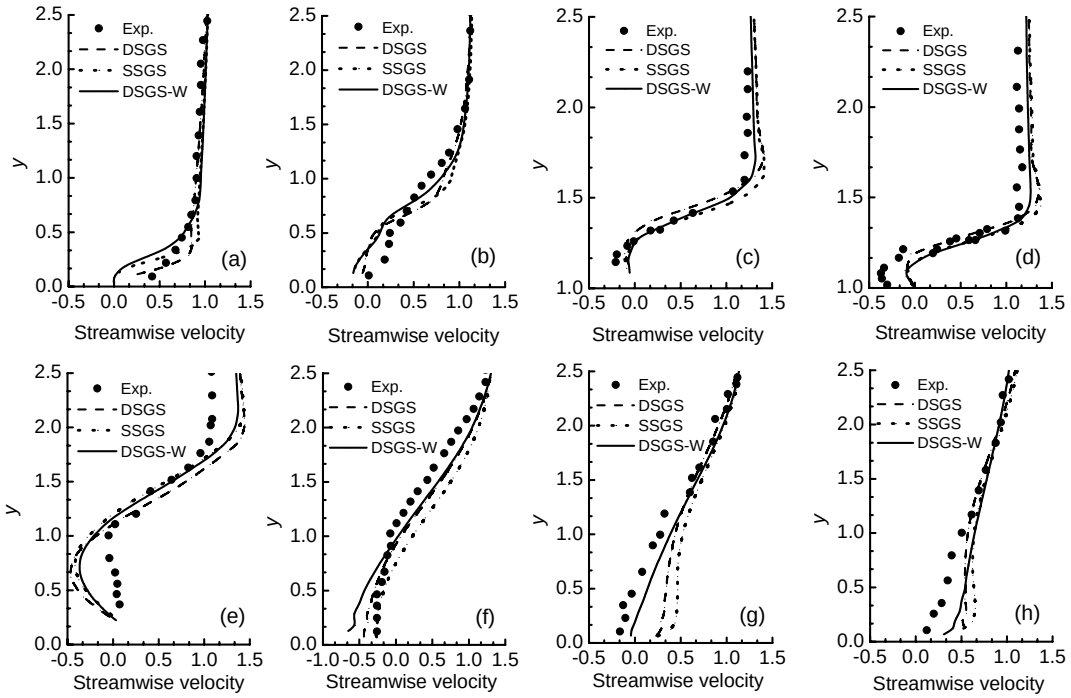

Fig. 4 Comparison of velocity predictions and measurements at different axial locations of the square rib
(a) x=−2.5; (b) x=−0.9; (c) x=0; (d) x=0.5; (e) x=1.5; (f) x=6.0; (g) x=9.5; (h) x=12.5. Exp.: results from Crabb *et al*. (1977)

at y<1.2. The DSGS-W case performs a little better than the other two cases. When x=1.5, the three cases show inaccurate predictions at y<1.0 and y>2.0. The DSGS-W case has a better trend than the others. When x=6.0, the DSGS-W case has a better prediction at y>0.8, but a worse prediction at y<0.8. When x=9.5, the DSGS-W case has by far the best prediction with experimental results than the others. When x=12.5, the three cases agree with the experimental results at y>1.2, and the DSGS-W case has a better performance

near the wall. When x=0.0 and x=0.5 on top of the rib, DSGS-W also has a better agreement away from the wall. In conclusion, the results from the present methods predict the wind flow well compared with the experimental results, and the DSGS-W case has a better performance than the other two cases. However, the loss of accuracy near the wall is concerned with the coarse mesh near the wall.

5.2 Wind flow around a surface-mounted cube

Six numerical cases are applied with the DSGS model based on the present stabilized FEM with the Cabot near-wall model, and the parameters are shown in Table 1. The three cases, GR1, GR2, and GR3, are established for the results' grid independence, whilst the three cases, RE1, RE2, and RE3, are for the analysis of different Reynolds numbers.

Table 1 Summary of numerical simulations

Case	Δmin	Δmax	Number of grids	Re	Δt	T
GR1	0.10	1.0	34 314	3×10^4	0.02	200
GR2	0.05	0.5	356 689	3×10^4	0.02	200
GR3	0.02	0.2	802 562	3×10^4	0.02	200
RE1	0.05	0.5	356 689	5×10^4	0.02	200
RE2	0.05	0.5	356 689	1×10^5	0.02	200
RE3	0.05	0.5	356 689	2×10^5	0.02	200

Δmin: minimal grid size; Δmax: maximal grid size; Δt: time step; T: total time

For the case of the wind flow around a surface-mounted cube with the dimension of unit length, the 3D computational domain and the grid discretization of GR2 as a sample are shown in Fig. 5a. The location of the 3D cube and the size of the 3D domain are expressed by the slices corresponding to y=0.0 and x=0.0 shown in Figs. 5b and 5c, respectively. The computational domain in the present study is 22.5, 8.0, and 7.0 in x, y, and z directions, respectively, which is the same as Young *et al*. (2006). A no-slip boundary condition is imposed along the wall of z=0.0 and the surfaces of the cube, and u=1, v=0, and w=0 are prescribed along the inlet boundary of x=−7.0 and the upper boundary of z=7.0. A slip boundary condition is imposed along the side surfaces at y=−4.0 and y=4.0, and the outer boundary located downstream is given a pressure of zero. The domain is discretized by linear tetrahedral elements with a fine mesh near the cube to capture the various details of turbulence.

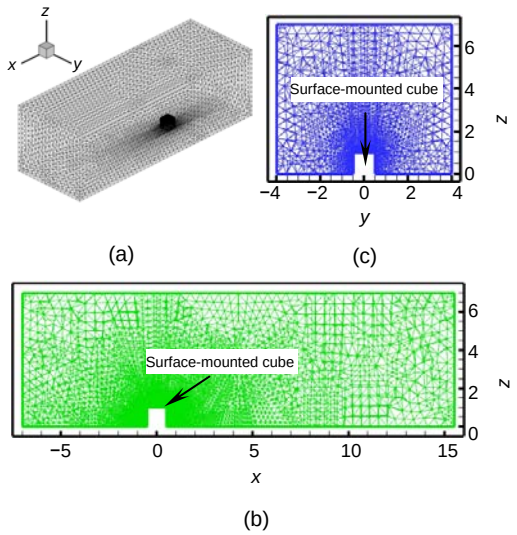

Fig. 5 Three-dimensional computational model
(a) Computational domain and mesh; (b) Slice from y=0.0; (c) Slice from x=0.0

Firstly we consider the velocity field around the cube. Fig. 6 presents the time-average streamwise velocity profiles at some typical positions around the cube from GR1, GR2, and GR3, comparing the present data with experimental results from Castro and Robins (1977). On top of the cube at x=0.0 and y=0.0, the predictions from GR2 and GR3 agree with the experimental results more closely than that from GR1, which indicated that the coarser grid case GR1 cannot catch the recirculation existing on top of the cube. The velocity values from the finer case GR3 are a little higher than the experimental results. For x=1.0 and y=0.0, the streamwise velocity from GR2 is well predicted, and the prediction from GR3 has a little disparity, while the prediction from GR1 loses accuracy within the near-wall region. Another interesting velocity profile at x=2.0 and y=0.0 is accurately predicted by GR3, and the cases GR1 and GR2 can also have good predictions. At the profile of x=2.0 and z=1.0, the three cases all predicted well the streamwise velocity but there are discrepancies for all of them. Note that the cases GR2 and GR3 could yield comparatively good results, while the case GR1 loses prediction within the near-wall region.

Table 2 shows the comparisons of the separation length (X_F) in front of the cube, the reattachment length (X_R) behind the cube as well as the mean and the root mean square (RMS) values of the drag

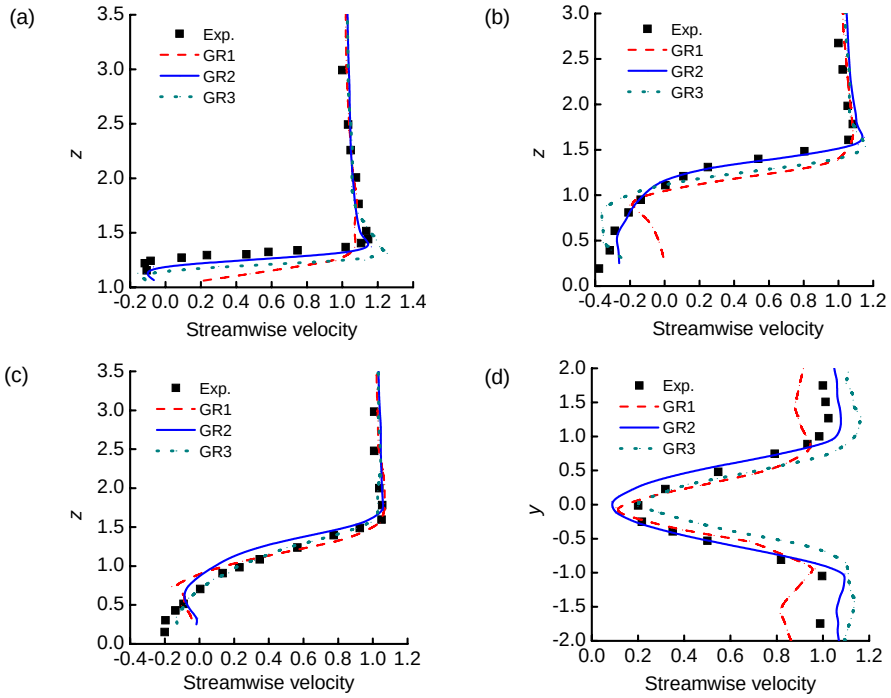

Fig. 6 Comparison of velocity predictions from GR1, GR2, and GR3 with measurements around a cube
(a) x=0.0, y=0.0; (b) x=1.0, y=0.0; (c) x=2.0, y=0.0; (d) x=2.0, z=1.0. Exp.: results from Castro and Robins (1977)

Table 2 Comparison of characteristic parameters between present studies and experiments and numerical studies by others

Model	Number of grids	X_F	X_R	$C_{D,t}$	$C_{D,rms}$
Experiment[a]	–	1.04	1.61	–	–
Smagorinsky[b]	165×65×97	1.29	1.70	–	–
Dynamic[b]	165×65×97	0.998	1.432	–	–
Smagorinsky[b]	144×58×88	0.808	1.722	–	–
Smagorinsky[c]	192×64×96	1.05	1.65	–	–
RANS[d]	500 000	0.64	3.32	–	–
URANS[d]	500 000	0.73	1.88	–	–
Dynamic1[b]	162×66×98	1.12	1.45	1.18	0.055
Dynamic2[b]	162×66×98	1.09	1.54	1.17	0.057
Dynamic1[b]	210×66×114	1.10	1.45	1.17	0.047
Dynamic2[b]	210×66×114	1.14	1.44	1.15	0.051
GR1[e]	34 314	0.80	1.89	0.45	0.006
GR2[e]	356 689	0.91	1.81	0.98	0.025
GR3[e]	802 562	1.05	1.69	0.94	0.039
RE1[e]	356 689	0.95	1.90	0.99	0.023
RE2[e]	356 689	0.93	1.85	1.00	0.023
RE3[e]	356 689	0.96	1.87	0.98	0.020

[a] Martinuzzi and Tropea, 1993; [b] Krajnovic and Davidson, 2002; [c] Shah and Ferziger, 1997; [d] Iaccarino and Durbin, 2000; [e] Present methods. X_F: separation length; X_R: reattachment length; $C_{D,t}$ and $C_{D,rms}$: the mean and the root mean square (RMS) values of drag coefficient

coefficient ($C_{D,t}$ and $C_{D,rms}$) using present numerical studies with experiments and numerical simulations by others. The best agreement with the experimental results for X_F and X_R is from the fine grid case GR3, and the present predictions are worsened with the coarseness of the grid. Compared with the results from others, X_F and X_R from GR2 using a dynamic model are acceptable. There is no experimental study on the drag coefficient of a surface-mounted cube, so we compare C_D and $C_{D,rms}$ with another numerical LES study by Krajnovic and Davidson (2002). It appears that GR1 fails to predict $C_{D,t}$ and $C_{D,rms}$ while GR2 and GR3 obtain reasonable results compared with Krajnovic and Davidson (2002). With the increase of grid numbers, $C_{D,rms}$ is increased but the values are still smaller than those from Krajnovic and Davidson (2002). By comparing the data from cases GR2, RE1, RE2, and RE3, different Re of 3×10^4, 5×10^4, 1×10^5, and 2×10^5 are applied, and the characteristic parameters of X_F, X_R, $C_{D,t}$, and $C_{D,rms}$ are similar to each other in this range of Reynolds numbers.

As shown in Fig. 7, results of the time histories of the drag coefficient C_D from GR1, GR2, and GR3 are consistent with those in Table 2. The coarse grid case GR1 fails to predict the mean drag coefficient

$C_{D,t}$ (Table 2), and there is nearly no oscillation of the time history of C_D (Fig. 7). The mean drag coefficients $C_{D,t}$ from GR2 and GR3 show reasonable agreement with references as shown in Table 2, and the time histories of C_D from GR2 and GR3 manifest disordered oscillation without major frequencies.

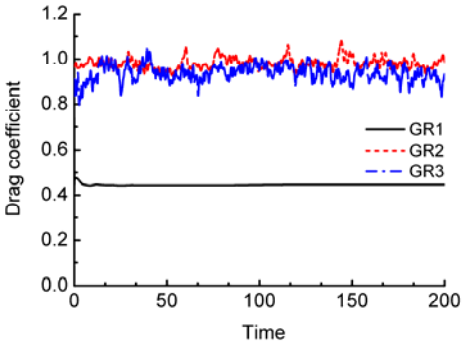

Fig. 7 Time histories of drag coefficient C_D of the cube from GR1, GR2, and GR3

Subsequently the general structures of the wind flow around the surface-mounted cube are characterized by describing the velocity fields of *x*-*z* plane at *y*=0.0 and *x*-*y* plane at *z*=0.5 using steamlines, streamwise velocity, and vorticity distributions as shown in Figs. 8 and 9. Here we use the prediction from the medium grid case GR2 as a sample.

As shown in Fig. 8, the recirculation region associated with the necklace vortex is obvious upstream of the cube with its center located at *x*=−1.1 and *z*=0.15 approximately. Above the necklace vortex, a stagnation point on the upwind surface is located at approximately *z*=0.8. Note that strong *y*-directional vorticity exists at the windward corner and spreads downstream, due to the separation at the front corner (Fig. 8c). The data obtained in the present study is very similar to the experimental study by Lim *et al*. (2009). Fig. 9 shows that the time averaged flow field

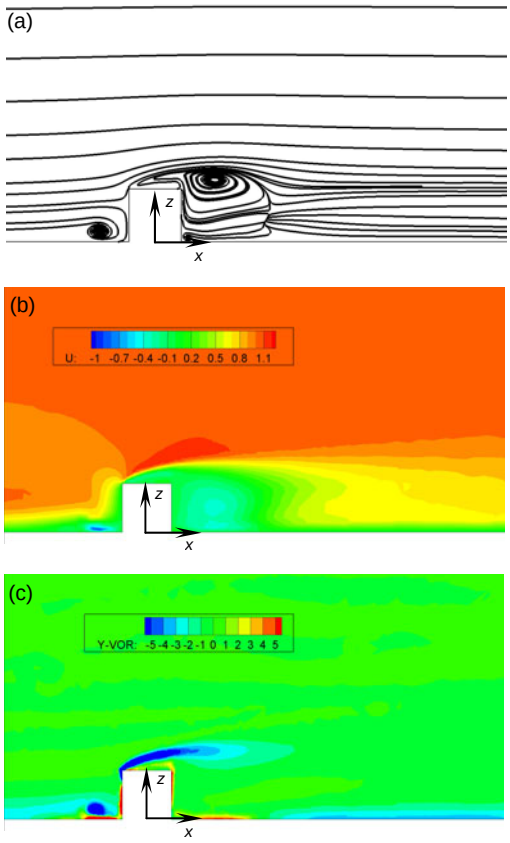

Fig. 8 Mean flow field for the wind flow around a surface-mounted cube on *x*-*z* plane at *y*=0.0
(a) Streamline distribution, (b) Streamwise velocity field; (c) *y*-directional vorticity distribution

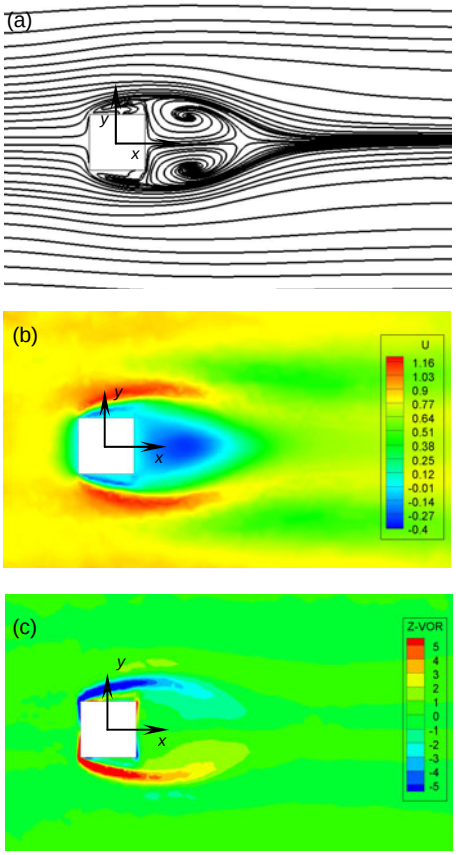

Fig. 9 Mean flow field for the wind flow around a surface-mounted cube on *x*-*y* plane at *z*=0.5
(a) Streamline distribution, (b) Streamwise velocity field; (c) *z*-directional vorticity distribution

is symmetrical with the stagnation point in the middle of the upwind surface. It is clearly visible that there are two pairs of recirculation regions on the lateral and rear of the cube. The strong *z*-directional vorticity occurs at the windward corners and spreads downstream symmetrically (Fig. 9c).

Previously the main features of turbulent flow around surface-mounted obstacles were analyzed in detail using smoke and oil-film visualization (Hunt *et al*., 1978; Martinuzzi and Tropea, 1993). Recently, the application of the numerical simulation such as LES method for such problems has become increasingly popular (Song, 1993; Chikamatsu *et al*., 2003; Kakuda, 2004). Based on the previous investigation, the significant vortex structure for the wind flow around a surface-mounted cube was constructed theoretically.

The time-averaged streamline distributions at typical positions around a surface-mounted cube using the present method are shown in Fig. 10. The vortex occurs within the windward circulation zone with the streamlines spreading symmetrically downstream along the lateral sides of the cube, which can be marked F (Fig. 10a). The vortex T is visualized by Fig. 10b at the circulation zone on top of the cube. Fig. 10c shows the horseshoe vortex generated at the lateral sides of the cube due to the separation occurring at the front of the lateral sides, which can be marked S. Finally, a pair of vortices R behind the cube can be seen, which is caused by the circulation from top and side faces, and the axes of the vortices are not vertical but like an arch (Fig. 10d). All of these above are established as four types of vortices existing around a cube, named as F, T, S, and R, which were confirmed by Sousa (2002).

Fig. 11 shows the time-averaged iso-surfaces of *z*- and *y*-directional vorticities. The *z*-directional vorticity is mainly located on the lateral sides of the cube and distributed symmetrically identified as vortex S due to the separation which occurred from the vertical edges upwind (Fig. 11a). The *y*-directional vorticity is

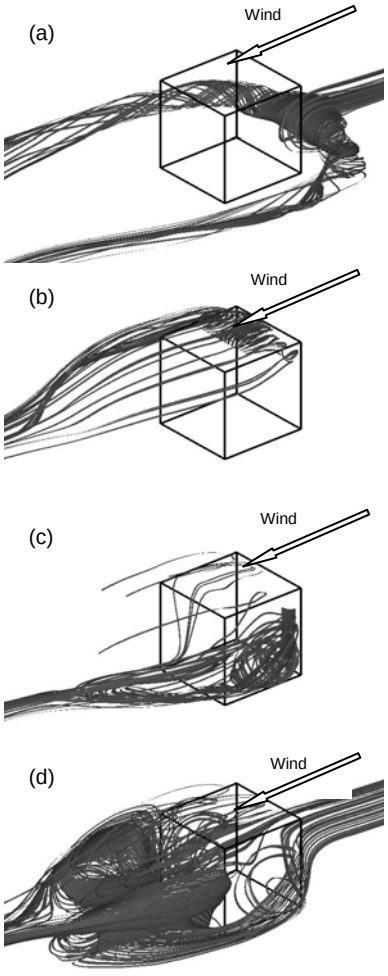

Fig. 10 Time-averaged streamline distributions around a surface-mounted cube

(a) Vortex F in front of the cube; (b) Vortex T on top of the cube; (c) Vortex S on the lateral side of the cube; (d) Vortex R behind the cube

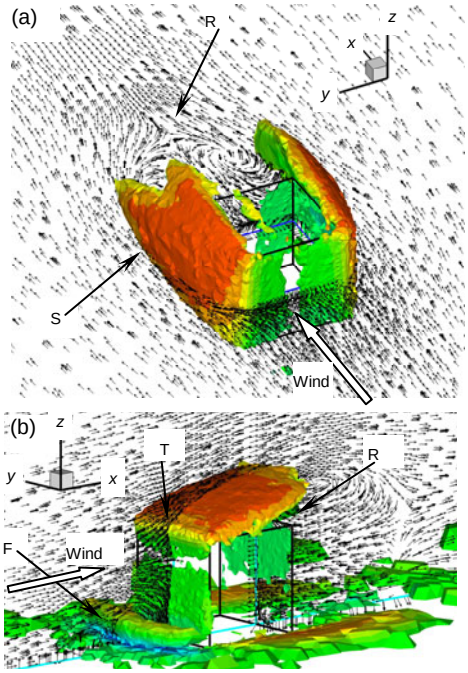

Fig. 11 Time-averaged iso-surfaces of *z*-directional (a) and *y*-directional (b) vorticities

mainly located at the bottom corner upwind and the top side of the cube due to the separations which occurred on the upwind ground and horizontal edge upwind respectively, identified as vortex F and vortex T (Fig. 11b). The vortex R behind the cube is hard to be shown using iso-surface of vorticity since the vorticity is very small, but we still can infer its existence by checking the velocity vector behind the cube. We can observe both *z*- and *y*-directional vorticities behind the cube from Fig. 11, which could reasonably be regarded as the complicated arch type vortex R.

6 Conclusions

In this paper, a stabilized finite element technique is implemented using a three-step FEM and SUPG stabilized method for LES to overcome the instabilities of the traditional FEM in prediction of flow with a high Reynolds number. For the numerical example of a 2D wind flow over a square rib at $Re=4.2\times10^5$, the DSGS model implemented by the present stabilized method with Cabot near-wall model yields more stable solutions and provides more reasonable results than the DSGS and SSGS methods without the Cabot near-wall model. Furthermore, numerical prediction of 3D wind flow around a surface-mounted cube performed by the present DSGS method with Cabot near-wall model obtains stable and satisfactory solutions, which show agreement with experimental results. Finally, four typical significant vortex structures for wind flow around a surface-mounted cube are predicted by the present numerical method, and proved to be precise based on previous investigations. In conclusion, it is demonstrated that the numerical method can appropriately model the highly turbulent flow problems with complex structural geometries. In addition, the wind field can be reasonably described even under a comparatively coarse mesh.

References

Brooks, A.N., Hughes, T.J.R., 1982. Streamline upwind Petrov-Galerkin formulation for convection dominated flows with particular emphasis on the incompressible Navier-Stokes equations. *Computer Methods in Applied Mechanics and Engineering*, **32**(1-3):199-259. [doi:10.1016/0045-7825(82)90071-8]

Cabot, W., 1996. Near-Wall Models in Large Eddy Simulations of Flow Behind a Backward-Facing Step. Annual Research Briefs, Center for Turbulence Research, Stanford, CA, USA, p.199-210.

Castro, I.P., Robins, A.G., 1977. The flow around a surface-mounted cube in uniform and turbulent streams. *Journal of Fluid Mechanics*, **79**(2):307-335. [doi:10.1017/S0022112077000172]

Chikamatsu, S., Nozawa, K., Tamura, T., 2003. Large Eddy Simulation of Turbulent Flows and Pressures on a Cube in an Artificial Wind. 11th International Conference on Wind Engineering, Texas, USA.

Crabb, D., Durao, D.F.G., White, J.H., 1977. Velocity Characteristic in the Vicinity of a Two Dimensional Rib. Proceeding of the 4th Brazilian Congress on Mechanical Engeering, Florianopolis, Brazil, p.47-58.

Deardorff, J.W., 1970. A numerical study of three-dimensional turbulent channel flow at large Reynolds numbers. *Journal of Fluid Mechanics*, **41**(2):453-480. [doi:10.1017/S0022112070000691]

Dettmer, W., Peric, D., 2006. A computational framework for fluid-structure interaction: finite element formulation and applications. *Computer Methods in Applied Mechanics and Engineering*, **195**(41-43):5754-5779. [doi:10.1016/j.cma.2005.10.019]

Germano, M., Piomelli, U., Moin, P., Cabot, H., 1991. A dynamic subgrid-scale eddy viscosity model. *Physics of Fluids*, **3**(7):1760-1765. [doi:10.1063/1.857955]

Hughes, T.J.R., Franca, L.P., Balestra, M., 1986. A new finite element formulation for computational fluid dynamics: V. Circumventing the Babuška-Brezzi condition: a stable Petrov-Galerkin formulation of the Stokes problem accommodating equal-order interpolations. *Computer Methods in Applied Mechanics and Engineering*, **59**(1):85-99. [doi:10.1016/0045-7825(86)90025-3]

Hunt, J.C.R., Abell, C.J., Peterka, J.A., Woo, H., 1978. Kinematical studies of the flows around free or surface-mounted obstacles: applying topology to flow visualization. *Journal of Fluid Mechanics*, **86**(1):179-200. [doi:10.1017/S0022112078001068]

Iaccarino, G., Durbin, P., 2000. Unsteady 3D RANS Simulations Using the v^2-f Model. Annual Research Briefs, Center for Turbulence Research, Stanford, CA, USA, p.263-269.

Itoh, Y., Tamura, T., 2008. Large eddy simulation of turbulent flows around bluff bodies in overlaid grid systems. *Journal of Wind Engineering and Industrial Aerodynamics*, **96**(10-11):1938-1946. [doi:10.1016/j.jweia.2008.02.065]

Jansen, K., 1994. Unstructured-Grid Large-Eddy Simulation of Flow over an Airfoil. Annual Research Briefs, Center for Turbulence Research, Stanford, CA, USA, p.161-175.

Jansen, K.E., 1999. A stabilized finite element method for computing turbulence. *Computer Methods in Applied Mechanics and Engineering*, **174**(3-4):299-317. [doi:10.1016/S0045-7825(98)00301-6]

Jiang, C.B., Kawahara, M., 1993. A three step finite element method for unsteady incompressible flows. *Computational Mechanics*, **11**(5-6):355-370. [doi:10.1007/BF00350093]

Jimenez, A., Crespo, A., Migoya, E., Garcia, J., 2008. Large-eddy simulation of spectral coherence in a wind turbine wake. *Environmental Research Letters*, **3**(1):015004. [doi:10.1088/1748-9326/3/1/015004]

Kakuda, K., 2004. Finite element computations of flow around a wall-mounted cube. *International Journal of Computational Fluid Dynamics*, **18**(5):393-399. [doi:10.1080/10618560310001523 71]

Krajnovic, S., Davidson, L., 2002. Large-eddy simulation of the flow around a bluff body. *AIAA Journal*, **40**(5):927-936. [doi:10.2514/2.1729]

Lilly, D.K., 1992. A proposed modification of the Germano subgrid-scale closure method. *Physics of Fluids*, **4**(3): 633-635. [doi:10.1063/1.858280]

Lim, H.C., Thomas, T.G., Castro, I.P., 2009. Flow around a cube in a turbulent boundary layer: LES and experiment. *Journal of Wind Engineering and Industrial Aerodynamics*, **97**(2):96-109. [doi:10.1016/j.jweia.2009.01.001]

Martinuzzi, R., Tropea, C., 1993. The flow around surface-mounted, prismatic obstacles placed in a fully developed channel flow. *Journal of Fluids Engineering*, **115**(1):85-92. [doi:10.1115/1.2910118]

Moin, P., Jimenéz, J., 1993. Large Eddy Simulation of Complex Turbulent Flows. AIAA 24th Fluid Dynamics Conference, Orlando, USA, AIAA-93-3099.

Popiolek, T.L., Awruch, A.M., Teixeira, P.R.F., 2006. Finite element analysis of laminar and turbulent flows using LES and subgrid-scale models. *Applied Mathematical Modelling*, **30**(2):177-199. [doi:10.1016/j.apm.2005.03.019]

Shah, K.B., Ferziger, J.H., 1997. A fluid mechanicians view of wind engineering: large eddy simulation of flow past a cubic obstacle. *Journal of Wind Engineering and Industrial Aerodynamics*, **67-68**:211-224. [doi:10.1016/S0167-6105(97)00074-3]

Smagorinsky, J., 1963. General circulation experiment with the primitive equations I. the basic experiment. *Monthly Weather Review*, **91**(3):99-164. [doi:10.1175/1520-0493(1963)091<0099:GCEWTP>2.3.CO;2]

Song, C.C., 1993. Computation of wind flow around a tall building and the large-scale vortex structure. *Journal of Wind Engineering and Industrial Aerodynamics*, **46-47**: 219-228. [doi:10.1016/0167-6105(93)90287-X]

Sousa, J.M.M., 2002. Turbulent flow around a surface-mounted obstacle using 2D-3C DPIV. *Experiments in Fluids*, **33**(6):854-862. [doi:10.1007/s00348-002-0497-5]

Tejada-Martínez, A.E., Jansen, K.E., 2004. A dynamic Smagorinsky model with dynamic determination of the filter width ratio. *Physics of Fluids*, **16**(7):2514-2518. [doi:10.1063/1.1738415]

Tezduyar, T.E., 2007. Finite elements in fluids: stabilized formulations and moving boundaries and interfaces. *Computers & Fluids*, **36**(2):191-206. [doi:10.1016/j.compfluid.2005.02.011]

Uchida, T., Ohya, Y., 2003. Large-eddy simulation of turbulent airflow over complex terrain. *Journal of Wind Engineering and Industrial Aerodynamics*, **91**(1-2):219-229. [doi:10.1016/S0167-6105(02)00347-1]

Young, D.L., Eldho, T.I., Chang, J.T., 2006. Large eddy simulation of turbulent flows in external flow fields using three-step FEM-BEM model. *Engineering Analysis with Boundary Elements*, **30**(7):564-576. [doi:10.1016/j.enganabound.2006.02.004]